Journal of
Synchrotron
Radiation

ISSN 1600-5775

Received 25 September 2013
Accepted 8 January 2014

Expected thermal deformation and wavefront preservation of a cryogenic Si monochromator for Cornell ERL beamlines

Rong Huang,[a]* Donald H. Bilderback[a,b] and Kenneth Finkelstein[a]

[a]Cornell High Energy Synchrotron Source, Cornell University, 161 Synchrotron Drive, Ithaca, NY 14853, USA, and [b]School of Applied Engineering Physics, Cornell University, Ithaca, NY 14853, USA. *E-mail: rh66@cornell.edu

Cornell energy-recovery linac (ERL) beamlines will have higher power density and higher fractional coherence than those available at third-generation sources; therefore the capability of a monochromator for ERL beamlines has to be studied. A cryogenic Si monochromator is considered in this paper because the perfect atomic structure of Si crystal is needed to deliver highly coherent radiation. Since neither the total heat load nor the power density alone can determine the severity of crystal deformation, a metric called modified linear power density is used to gauge the thermal deformation. For all ERL undulator beamlines, crystal thermal deformation profiles are simulated using the finite-element analysis tool *ANSYS*, and wavefront propagations are simulated using *Synchrotron Radiation Workshop*. It is concluded that cryogenic Si monochromators will be suitable for ERL beamlines in general.

Keywords: cryogenic monochromator; energy-recovery linac; crystal thermal deformation; wavefront preservation; X-ray optics.

1. Introduction

Future energy-recovery linac (ERL) sources, with smaller source emittance and higher X-ray coherence (Bilderback *et al.*, 2010) than available at existing third-generation sources, need excellent optics to preserve the high quality of the X-ray beam. At the proposed Cornell ERL, 5 m- and 25 m-long undulators are expected to generate radiation with extremely low divergence and very high power density and therefore the potential thermal deformation of monochromator crystals and the effect on wavefront distortions have to be carefully studied. Similar studies may also be needed for future high-coherence beamlines of ultimate storage rings.

Both liquid-nitrogen (LN_2) cooled silicon and water-cooled diamond crystals have been successfully utilized at third-generation beamlines, with cryogenic Si monochromators more widely used because perfect Si crystals are available in large dimensions. For future ERL beamlines, perfect monochromator crystals are required to deliver the highly coherent beam, therefore we focus our study on Si(111) monochromators. For cryogenic cooled Si, it has been realised that generally there is not much difference in monochromator performance between contact cooling and internal cooling (Chumakov *et al.*, 2004; Zhang *et al.*, 2003). It was also concluded, in general, that a crystal block has a better capability of dissipating heat than a crystal with a thin web cut underneath the crystal reflecting surface (Rogers *et al.*, 1996; Lee *et al.*, 2000; Tajiri *et al.*, 2001). Thus, for the ERL beamlines, we perform thermal analysis for a LN_2-cooled Si(111) block with dimensions of 30 mm by 30 mm by 80 mm, with the assumption of contact-cooling through indium foils and copper blocks clamped on two sides, similar to designs initially studied at SPring-8 (Tamasaku *et al.*, 2002) and ESRF (Chumakov *et al.*, 2004) and now used by most commercial designs. The consequence of both crystal thermal deformation and wavefront changes by heat load is studied in this paper.

In the following, we briefly describe the radiation feature of ERL undulators. We use a function of modified linear power density to describe Si crystal thermal deformation independent of the specifics of synchrotron facilities and beamlines. We use the finite-element analysis tool *ANSYS* to calculate crystal deformation profiles for eight different undulator beamlines and parameters of the proposed Cornell ERL, and estimate wavefront distortion by simulating how the deformed crystal affects the one-to-one focusing of an ERL source using *Synchrotron Radiation Workshop* (*SRW*) (Chubar *et al.*, 2002). The suitability of a cryogenic Si(111) monochromator for Cornell ERL beamlines is summarized.

2. Radiation power from ERL undulators

Table 1 summarizes the parameters relevant to undulator radiation at the proposed 5.0 GeV Cornell ERL (Bilderback *et al.*, 2010). This machine would operate at two different

Table 1
Cornell ERL source parameters.

Mode	$\Delta E/E$ (%)	Current (mA)	$\varepsilon_x/\varepsilon_y$ (nm rad)	σ_x (μm) (S/L)†	σ_y (μm) (S/L)†	σ_x' (μrad) (S/L)†	σ_y' (μrad) (S/L)†
High flux	0.0186	100	0.031/0.025	4.95/11.1	4.45/9.95	6.22/2.78	5.59/2.50
High coherence	0.0088	25	0.013/0.011	3.217/7.19	2.904/6.49	4.042/1.81	3.649/1.63

† Source dimensions are calculated with β functions equal to undulator length over 2π, and 'S/L' stands for short/long undulators.

currents, 25 and 100 mA, corresponding to high coherence mode and high flux mode, respectively. While at lower current the lower source emittance will yield a higher percentage of coherent X-rays, at high current the source will provide higher X-ray flux. Because the ERL source is round, with very low emittance in both transverse directions, the so-called Delta undulator (Temnykh, 2008) can offer the flexibility of switching undulator polarization between linear and helical modes. Both 5 m- and 25 m-long undulators with 19 mm period will be used. In the end, there will be eight different beamline conditions with different combinations of machine current, undulator polarization mode and undulator length. The main features of ERL undulator radiation pertinent to thermal analysis can be summarized as follows.

Table 2
On-axis maximum power density of Cornell ERL beamlines under high flux mode.

	ERL planar	ERL planar	ERL helical	ERL helical
N	1315	263	1315	263
L (m)	25	5	25	5
λ_u (m)	0.019	0.019	0.019	0.019
K	2.2218	2.2218	$Kx = Ky = 0.707$	$Kx = Ky = 0.707$
$dP/d\Omega$ (W mrad^{-2})	1.10×10^6	2.18×10^5	3.40×10^5	6.80×10^4

2.1. On-axis power density

Because of the very low source emittance, electron source divergence is much smaller than the angular opening of power radiated in both transverse directions; therefore, the radiated power can be calculated with formulas of a zero-emittance source (for example, Walker, 1998; Onuki & Elleaume, 2003). The on-axis power density from a planar undulator is

$$\frac{dP}{d\Omega}\left[\text{W mrad}^{-2}\right] = 0.116\, E^4\, NIK\, G(K)/\lambda_u \qquad (1)$$

with

$$G(K) = K\left(K^6 + \tfrac{24}{7}K^4 + 4K^2 + \tfrac{16}{7}\right)/(1+K^2)^{7/2},$$

where K is the undulator deflection parameter, E is the electron energy in GeV, I is the source current in Amperes, N is the number of undulator periods, and λ_u is the undulator period in meters. For helical undulators, the on-axis power density is

$$\frac{dP}{d\Omega} = 0.531\, E^4\, I\, \frac{L}{\lambda_u^2}\, \frac{K^2}{\left(1+K^2\right)^3}, \qquad (2)$$

where L is the undulator length in meters. Planar undulator maximum on-axis power density increases with K, but helical undulator on-axis power density reaches a maximum when $K = 0.707$.

The on-axis power densities of ERL beamlines with a machine current of 100 mA are listed in Table 2, and will be smaller by a factor of four in the high coherence mode at 25 mA. As a comparison, the APS undulator A on-axis power density is only about 1.6×10^5 W mrad^{-2} under the closed-gap condition (Dejus *et al.*, 2002), and the powerful PETRA III 10 m-long U32 undulator maximum on-axis power density is about 3.0×10^5 W mrad^{-2} (Balewski, 2008). Thus, except for the 5 m-long helical undulators, Cornell ERL beamlines have higher on-axis power density compared with what is normally encountered at third-generation sources.

2.2. Radiation central cone

When synchrotron source emittance, $\varepsilon = \sigma * \sigma'$, is small and comparable with the undulator natural size in phase space, $\varepsilon_r = \sigma_r * \sigma_r'$, X-ray brilliance is maximized when $\sigma/\sigma_r = \sigma'/\sigma_r'$. This implies that the optimized β function at the undulator is related to undulator length (Wiedemann, 2003). However, given the fact that the phase space density of a zero-emittance undulator source is not Gaussian, and the electron beam phase space distribution of a linac accelerator can be non-Gaussian, the optimized β function becomes application-dependent, *e.g.* whether to optimize peak brilliance or r.m.s. brilliance (Bazarov, 2012). Currently the main tool we use to calculate undulator radiations is *SPECTRA* (Tanaka & Kitamura, 2001); we choose $\beta = L/2\pi$ as optimal to match the undulator natural size used in *SPECTRA*, which is $\sigma_r = (2\lambda L)^{1/2}/4\pi$, $\sigma_r' = (\lambda/2L)^{1/2}$, as calculated by Kim (1988).

On a synchrotron beamline, a power slit can be used to limit the incident power to the monochromator to an acceptable level. For an ERL beamline, however, because of the high degree of coherence, a slit may produce interference fringes downstream when it cuts into the central cone, even for the so-called 'high flux' mode of the ERL operation, as shown in Fig. 1. Although the fringes may not cause problems for every application, for thermal analysis in this paper we let the heat-limiting aperture upstream of the monochromator always accepts the entire central cone. This eliminates downstream fringes, as verified using wavefront simulation code *SRW*. Since the central cone opening, as shown in Table 3 for slit size, is much smaller than the opening of radiated power, the on-axis power density can be used to approximate the radiation power on the monochromator. Using *SPECTRA* (version 9.0), we find that, for all ERL cases studied in this paper, there

Table 3
Conditions and results of *ANSYS* simulations for ERL beamlines.

Beam current (mA)	Slit size (H × V) (mm)	Distance to source (m)	Radiation power FWHM (H × V) (mm)	Power in central cone (W)	K	First harmonic energy (keV)	MLPD (W mm^{-1})	T_{max} (K)	Weighted slope error (μrad)	Displacement (nm)†
25 m-long planar undulator										
100	0.85 × 0.85	45	16.9 × 5.9	391	2.22	3.6	310	311	80	99.0
25	0.85 × 0.85	45	16.9 × 5.9	98	2.22	3.6	78	102	1.35	−2.06
100	0.75 × 0.75	45	8.02 × 5.6	141	1.06	8.0	70	126	1.94	−4.28
25	0.75 × 0.75	45	8.02 × 5.6	35	1.06	8.0	17	88.6	0.61	−1.34
5 m-long planar undulator										
100	1.5 × 1.5	35	13.2 × 4.6	401	2.22	3.6	178	194	12.5	25.5
25	1.5 × 1.5	35	13.2 × 4.6	101	2.22	3.6	45	95.2	0.9	−2.63
100	1.3 × 1.3	35	6.3 × 4.4	140	1.06	8.0	40	107	1.47	−5.92
25	1.3 × 1.3	35	6.3 × 4.4	35	1.06	8.0	10	85.5	0.35	−1.42
25 m-long helical undulator										
100	0.75 × 0.75	45	8.1 × 8.1	95	0.707	8.33	47	116	2.05	−4.79
25	0.75 × .75	45	8.1 × 8.1	24	0.707	8.33	12	87.0	0.52	−1.25
5 m-long helical undulator										
100	1.3 × 1.3	35	6.3 × 6.3	94	0.707	8.33	27	99.8	1.25	−5.4
25	1.3 × 1.3	35	6.3 × 6.3	24	0.707	8.33	6.7	82.3	0.30	−1.19

† The maximum vertical displacement within the footprint area, with positive values representing convex deformation.

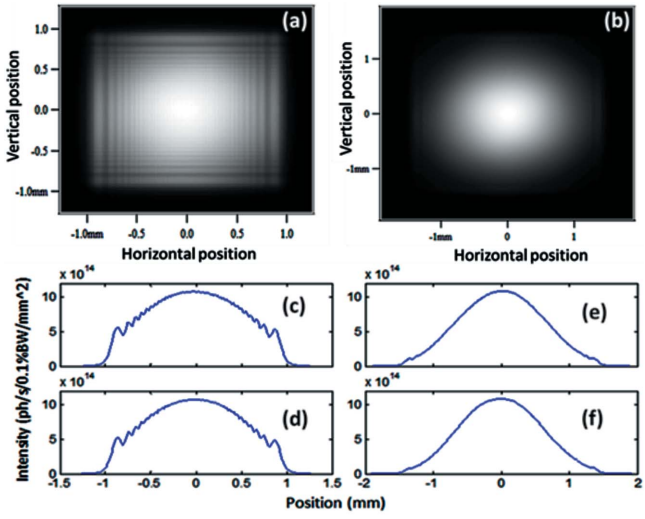

Figure 1
X-ray profiles calculated using *SRW* at 70 m from the source with the slit at 35 m, for the ERL 5 m planar undulator with first harmonic at 3.6 keV, in high flux mode. Using 1 mm × 1 mm slits, fringes will appear [(*a*) two-dimensional image; (*c*) horizontal profile; (*d*) vertical profile]. With 1.5 mm × 1.5 mm slits, fringes will mostly disappear [(*b*) two-dimensional image; (*e*) horizontal profile; (*f*) vertical profile].

are only 0.1% to 2.8% differences between the simulated power through white-beam slits and the on-axis power density multiplied by slit open areas.

2.3. Radiation power in the central cone

The undulator on-axis power density is proportional to the number of undulator periods, as shown in equation (1); on the other hand, the undulator central cone solid angle is inversely proportional to undulator length (Kim, 1988). For the Cornell ERL, the undulator period is the same for the 5 m- and 25 m-long undulators; this makes the radiated power in the central cone of both undulators about the same, as shown in Table 3. It can also be seen from Table 3 that, because of the small radiation angle of ERL undulators, the maximum radiated power in the central cone is only about 400 W, comparable with what is already observed at third-generation beamlines.

2.4. Spectral width of undulator harmonics

With the small ERL energy spread, a 25 m-long undulator, with period number as high as 1315, will have very narrow spectral features. However, as shown in Fig. 2, calculated with *SPECTRA*, although there is only minor spectral broadening by energy spread and source emittance, the main contributor to spectral width of the harmonics may come from the finite size of the central cone opening. A Si(111) monochromator would therefore significantly reduce the spectral width.

3. Modified linear power density and intensity weighted r.m.s. slope errors

It is believed that cryogenic Si crystal thermal deformation can be divided into three regimes (Zhang *et al.*, 2003). When heat load is small, slope errors caused by thermal deformation increase linearly with heating power. As power reaches a so-called transition region, the slope errors may not increase and could even decrease as heating power increases. Upon further increase of power to the non-linear region, slope errors increase dramatically as power goes up. Si thermal deformation depends not only on incident power but also the power density (Zhang *et al.*, 2003; Tamasaku *et al.*, 2002) and footprint shape (Chumakov *et al.*, 2004; Zhang *et al.*, 2003). This makes comparison of the severity of thermal deformation for different facilities and beamlines a complex task.

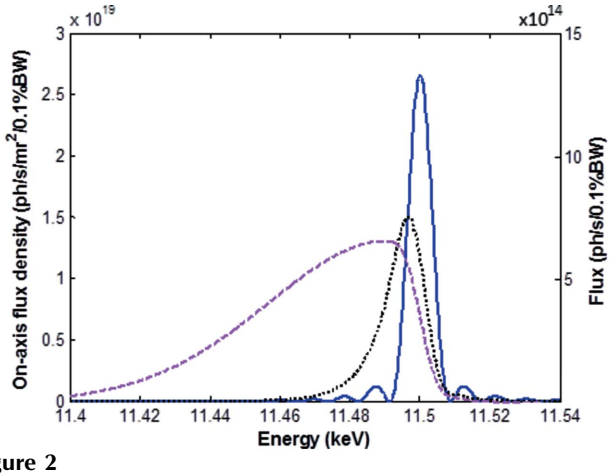

Figure 2
Calculated shift and broadening of the spectral peak by emittance and aperture, for the ERL 25 m planar undulator in high coherence mode. The solid line is the on-axis spectrum of the flux density with zero emittance and zero energy spread; the dotted line is the spectrum with finite emittance and energy spread, and the dashed line is the flux spectrum through a 600 µm-diameter pinhole located 45 m away from the source. The FWHMs of the curves are 7.8 eV, 12.3 eV and 50.5 eV, respectively.

By assuming that the thermal footprint on the crystal surface is much smaller than the crystal dimensions, we introduced an empirical metric called the 'modified linear power density' (MLPD) (Huang & Bilderback, 2012), a variable better for describing Si deformation independent of beamline specifics,

$$P_{\rm M} = [1 + \ln(L/W)/2.571]\ P/L, \qquad (3)$$

where P is the total accepted power, L and W are the length and width ($L \geq W$) of the X-ray footprint, and where a uniform surface heating within the footprint is assumed. MLPD determines the crystal thermal deformation caused by limited heat transfer within the crystal, based on a simple analytical model. Fig. 3(*a*) is a reproduction of the published *ANSYS* results for slope errors as a function of incident power for an ESRF monochromator, showing separated curves for different slit openings (Zhang *et al.*, 2003). Using MLPD as the variable, Fig. 3(*b*) shows the merging of the separated curves in Fig. 3(*a*), and even overlapping with *ANSYS* results for Cornell ERL beamlines. It can be seen from Fig. 3(*b*) that, roughly speaking, crystal deformation is in the linear region when MLPD is 50 W mm^{-1} or less, in the transition region when MLPD is 50–100 W mm^{-1}, and in the non-linear region when MLPD is 100 W mm^{-1} or higher, independent of facilities and beamlines.

At current synchrotron beamlines, the power distribution on a crystal surface may not be uniform. As an example of the widely used undulator A at APS working at K = 1.0, when the white-beam size is defined by a slit of 2.4 mm (H) by 1.0 mm (V) at 30 m to the source, the power density at a vertical edge is about 10% less than at the center, and at a horizontal edge it is about 20% less. To exaggerate the situation a little, Figs. 3(*c*) and 3(*d*) compare the simulated maximum temperatures and slope errors, for all the ERL cases, between uniform power on

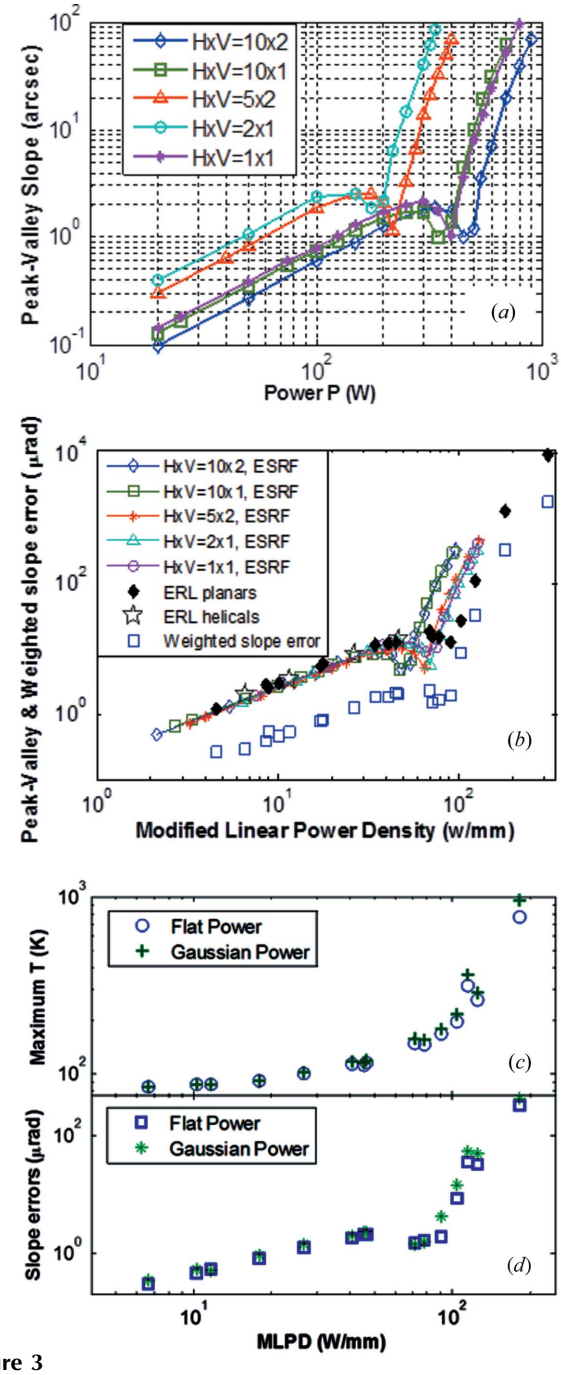

Figure 3
(*a*) Reproduction of ESRF finite-element analysis results for the LN_2-cooled Si monochromator for different slit openings. (*b*) The same ESRF results together with finite-element analysis results for Cornell ERL undulators, as a function of MLPD, under the surface heat assumption. The behavior of Si deformation in the 'linear region' can be described by a universal curve as a function of MLPD. The intensity-weighted slope errors are for Cornell ERL beamlines only. Simulated changes of maximum temperature and slope error caused by non-uniform power are shown in (*c*) and (*d*) with exaggerated assumption of 25% power density drop at the edge of the power distribution, with the total power matching ERL cases studied in this paper.

the crystal surface and the hypothetical Gaussian distribution with its power density at the edges 25% less than at the beam center. The non-uniform power distribution on the crystal surface will change the simulated temperature and slope

errors a little, especially around non-linear regions, but MLPD can still be used to evaluate the severity of crystal thermal deformation for undulator beamlines in general.

With rare exceptions (Kazimirov *et al.*, 2008; Zhang *et al.*, 2013), monochromator crystal thermal deformation is generally studied by measuring the rocking-curve broadening of the whole monochromatic beam passing through the monochromator. Simulated peak-to-valley slope errors in Figs. 3(*a*) and 3(*b*) are larger than that expected from measured rocking-curve broadening of the whole beam. Simple r.m.s. averaging of the slope errors over the beam footprint is not a good description because, for example for a monochromatic beam with Gaussian spatial distribution, the slope errors at the footprint edges contribute less to the measurement than slope errors at the footprint center where the intensity of the monochromatic beam is at maximum. Therefore, to better compare *ANSYS* simulated results with experimental data, we introduce intensity-weighted r.m.s. slope errors (or intensity-weighted slope errors for short), defined as

$$\alpha_{\rm RMS} = \left(\int I(x) \left\{ E(x) - {\rm mean}[E(x)] \right\}^2 {\rm d}x \Big/ \int I(x)\, {\rm d}x \right)^{1/2}, \quad (4)$$

where $I(x)$ is the position-dependent monochromatic X-ray intensity and $E(x)$ is the slope error *versus* position x on the surface. For simplicity, the integration in this paper is made along the centerline in the meridional direction, which is, in general, slightly larger than the average over the whole footprint area. The *ANSYS* simulated intensity-weighted slope errors for Cornell ERL beamlines, based on surface load assumption, are shown in Fig. 3(*b*) by squares. However, for planar undulators working at high K, volume heat must be used in *ANSYS* simulations because of the existence of high-energy harmonics in the radiation. Thus, all the intensity-weighted slope errors in Table 3 are the results with volume heat, and they only become unacceptably large, 12.5 µrad and 80 µrad, for 5 m and 25 m planar undulators working at maximum K, with MLPD larger than 100 W mm^{-1}. For MLPD < 100, the intensity-weighted slope errors given in Fig. 3(*b*) and Table 3 are small, comparable with the measured rocking-curve broadening observed at third-generation beamlines, for example, mostly in the range 0.7–5 µrad (Chumakov *et al.*, 2004). Even when simulated crystal deformation under volume heat gives different results than surface heat load, Table 3 shows that MLPD remains a useful indicator for severity of thermal deformation; in general, we need to keep MLPD at approximately 100 W mm^{-1} or less.

MLPD can also be used to estimate temperature increase of the crystal. When the assumption of crystal surface load is valid and when the MLPD is moderate, for example in the linear deformation range, the maximum temperature at the center of the footprint can be estimated using the formula (Huang & Bilderback, 2012)

$$T = T_k + (T_0 - T_k) \exp(0.0183 P_{\rm M}), \quad (5)$$

where T_0 is the crystal boundary temperature, normally around LN_2 temperature, T_k is a constant of 47.4 K, and $P_{\rm M}$ is the MLPD in units of W mm^{-1}.

Table 4
White-beam penetration depth inside the Si(111) crystal set for undulator first harmonic.

Undulator type	Helical	Planar	Planar
First-harmonic energy (keV)	8.3	8.0	3.6
Penetration depth (mm)†	0.018	0.048	1.35

† The X-ray intensity is e^{-1} of the incident X-ray intensity.

4. *ANSYS* simulation of ERL monochromator crystals

MLPD is the only universal variable we know of that can gauge cryogenic Si crystal deformation independent of facilities and beamlines. However, the *ANSYS* simulation is still needed for the following reasons: (i) MLPD is based on an assumption of crystal surface heat load; deviation of thermal deformation as a function of MLPD should be expected when the incident beam contains a high degree of high-energy X-rays that can penetrate deep into the crystal. This could be more significant for ERL beamlines since the beam footprint on the crystal is quite small; (ii) when deformation profiles are needed for analysis such as in wavefront simulation, *etc*.

Table 4 lists the X-ray power penetration depth inside the Si crystal in the direction perpendicular to the surface, with the incident beam spectrum calculated with *SPECTRA* and the crystal set at the Bragg angle for the first harmonic. For helical undulators and planar undulators working at moderate K, the penetration depth is only a few tens of micrometers; therefore, in the *ANSYS* model, we use a very fine 'biased sweep' mesh within the region underneath the beam footprint, with the smallest mesh size on the micrometer scale along the depth direction. For a planar undulator working at high K, the X-ray penetration depth can be more than 1 mm because of the increase of high-order harmonics in white beam (Kim, 1988), comparable with beam footprint dimensions at ERL beamlines. Meanwhile, for a planar undulator at high K, there is a much larger tail of intensity *versus* penetration depth than a simplified exponential decay curve of one decay constant, resulting from the broad spectral features of high-energy X-rays in the incident beam. The contact-cooling from two sides of the crystal is simulated with an effective cooling film coefficient of 5000 W m^{-2} K^{-1} (Zhang *et al.*, 2003), with boundary temperature assumed to be 80 K.

Fig. 4 shows the maximum crystal temperature for ERL helical beamlines at K = 0.707 (X-ray energy E = 8.32 keV), planar beamlines at K = 1.06 (first harmonic E = 8.0 keV) and K = 2.22 (first harmonic E = 3.6 keV), simulated with *ANSYS* with both surface heat and volume heat assumptions, using parameters in Table 3. It can be seen that surface heating is a good approximation for helical beamlines, or for planar beamlines working at moderate K; however, it is not suitable for planar beamlines working at high K. Especially within the non-linear region (MLPD $\simeq$ 100 or higher), the simulation result can be quite different if inappropriate models are used.

As typical examples, Fig. 5(*a*) shows the simulated crystal temperature for the 25 m-long planar undulator working at K = 2.22, with apparent asymmetric temperature profile, and

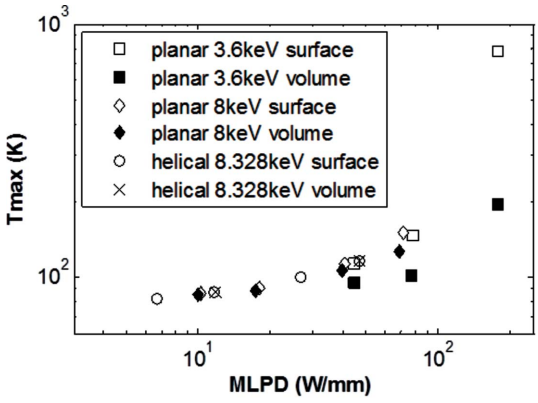

Figure 4
Difference of calculated maximum crystal temperatures using the surface heat model and the volume heat model. While such a difference is negligible for the helical undulators, and minor for planar undulators with first harmonic at 8.0 keV, the temperatures are profoundly different between the two models for the planar undulator at 3.6 keV. Also shown in the non-linear region where MLPD is greater than 100 W mm^{-1}, the result is much more sensitive to the heat load model used.

Fig. 5(*b*) shows the same undulator working at K = 1.06, with minor asymmetry on the temperature profile. Fig. 6 shows the crystal thermal displacement within the footprint area of the 25 m-long planar undulator working at K = 1.06, and the 25 m-long helical undulator working at K = 0.707. The *ANSYS* results for all ERL undulators working under extreme thermal conditions and for planar undulators at a moderate K = 1.06 are listed in Table 3. Among them, there are two cases where MLPD is too high: 310 W mm^{-1} for the 25 m planar undulator at maximum K and crystal Bragg angle at 3.6 keV, and 178 W mm^{-1} for the 5 m planar undulator at maximum K and crystal Bragg angle at 3.6 keV. For these cases the Si deformations are convex, indicated by positive displacement at the center of the footprint as shown in Table 3. For all other cases the deformations are concave, indicated by negative displacement in Table 3. The change of thermal curvature direction is expected by the well known fact that the Si thermal expansion coefficient becomes negative with temperature going below 125 K. The amplitudes of these relative displacements are mostly limited to a few nanometers. With volume heat, the deformation is also asymmetric along the meridional direction, but this only causes a very small 'tilting', normally about 1 µrad or less, along the beam direction. The intensity-weighted slope errors summarized in Table 3 are mostly around 2 µrad or less except for the two cases of very high MLPD. In general, the cryogenic monochromators will work fine for the high power density ERL beamlines, in terms of small or negligible rocking-curve broadening and maintaining flux throughput for Si(111) monochromators.

However, some mitigation is needed for the two cases with too high a MLPD. Very often, a planar undulator is set to maximum K for third- or higher-order harmonics rather than its first harmonic. Cornell ERL planar undulators at maximum K produce third-harmonic radiation at about 10.8 keV, where the incident beam footprint on the crystal will be three times as long as the footprint at the first harmonic. For the 5 m-long

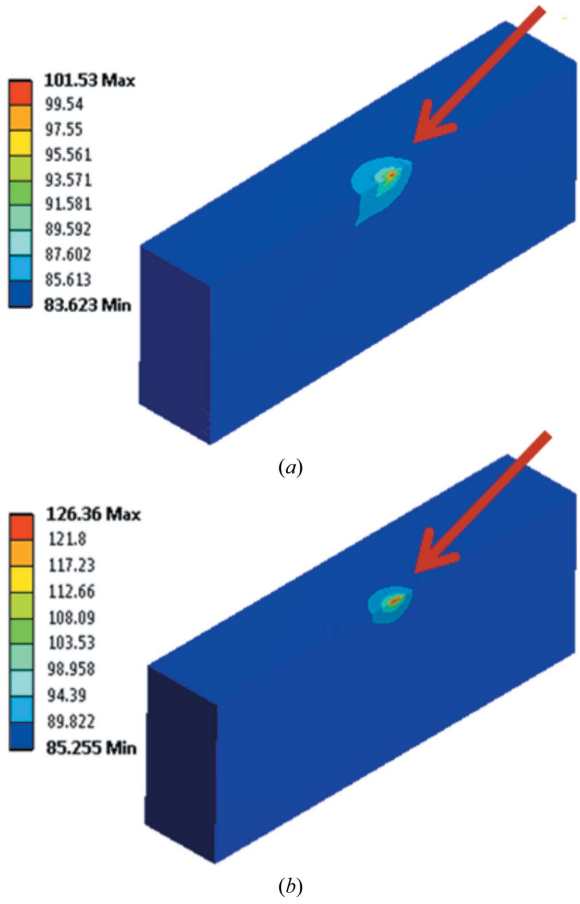

Figure 5
The asymmetry of Si crystal temperature distribution is more obvious for a planar undulator working at high deflection parameter K. White beam comes from upper-right corner to the crystal center in both graphs, as shown with red arrows. (*a*) Simulated temperature in a half crystal model, for the 25 m planar undulator at K = 2.22, 25 mA machine current. (*b*) Simulated temperature for a 25 m planar undulator at K = 1.06 with first harmonic at 8 keV, and 100 mA machine current.

planar undulator, the increased footprint reduces MLPD from 178 to 80 W mm^{-1}, corresponding to the transition region of thermal deformation. For the 25 m-long planar undulator, MLPD is reduced from 311 to 139 W mm^{-1}. If we also increase the monochromator distance, for example, from 45 m to 55 m, this reduces MLPD down to 114 W mm^{-1}. Because a significant portion of incident X-rays can penetrate deep into the crystal for the planar undulator at maximum K, even with MLPD slightly above 100 W mm^{-1}, *ANSYS* simulation (Fig. 7) predicts acceptable intensity-weighted slope errors of 3.4 µrad. On the other hand, the overall crystal temperature is greater than or equal to 94.4 K (Fig. 7), about 14.4 K higher than the cooling boundary temperature used in the simulation. This result is caused by a very high total power and limited cooling efficiency. Increase of the cooling efficiency, such as by internal cooling or increasing the crystal-copper contact area, will be helpful. Lastly, reducing the white-beam slit opening could be an option for some experiments. In short, there are ways to work around the high power load even for the worst-case heat load condition for ERL beamlines.

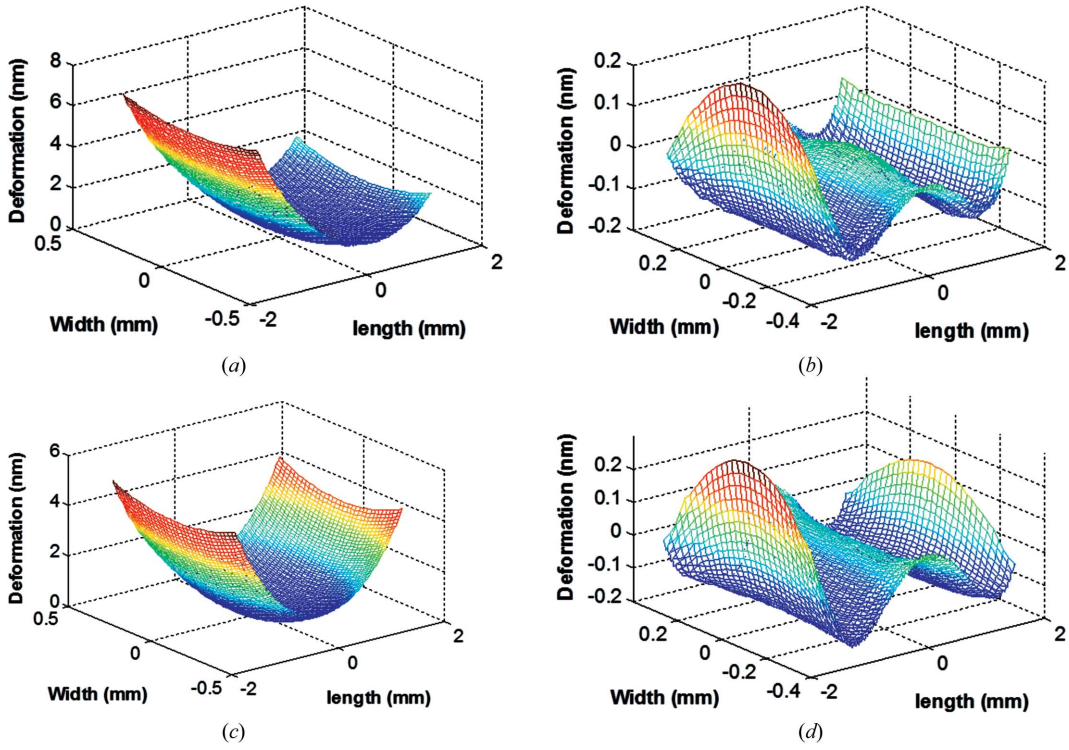

Figure 6
(*a*) Simulated vertical displacement of the crystal surface within the footprint area for the 25 m-long planar undulator working at $K = 1.06$, first harmonic at 8 keV, and a machine current of 100 mA. (*b*) Residual deformation after subtracting the toroidal curvatures of the crystal. (*c*) Crystal vertical displacement within the X-ray footprint area for a 25 m-long helical undulator working at $K = 0.707$, the maximum possible on-axis power condition, with machine current of 100 mA. (*d*) The residual deformation after subtracting the toroidal curvatures from the profile in (*c*).

5. Evaluation of wavefront preservation with *SRW*

The ultra-low emittance of an ERL source is advantageous to experiments relying on a high degree of transverse coherence and high-flux nano-focusing. While it is believed that coherence cannot be destroyed, and the loss of coherence (Vartanyants & Robinson, 2003; Robinson *et al.*, 2003) could be related to the finite resolution of the experiment system (Nugent *et al.*, 2003; Nesterets, 2008; Nugent, 2010), the increase of focal size by wavefront distortion can be studied quantitatively in a general way. Because of the large transverse coherence length of ERL undulator beams, geometric ray-tracing cannot correctly describe changes on beam propagation caused by optical errors. In this paper we evaluate the wavefront distortion for focusing with wavefront simulations.

When the slope errors of crystal thermal deformation are comparable with, or larger than, a Bragg reflection width, the numerical solution of the Takagi–Taupin equations is the appropriate way to describe X-ray diffraction by the crystal (Mocella *et al.*, 2001, 2003; Hoszowska *et al.*, 2001; Freund *et al.*, 2000). However, as described in the previous section, the crystal deformation for ERL beamlines is much smaller than the width of the Bragg reflection; therefore, its effect on wavefront propagation can be treated in the same way as surface errors on a reflecting mirror. Such errors can change the X-ray path length by

$$\Delta = 2h\sin(\alpha), \qquad (6)$$

where h is the crystal surface height displacement and α is the Bragg angle of the crystals. X-ray reflectivity is assumed to be not affected by the small slope errors. The Huygens–Fresnel principle can be used to simulate X-ray wavefront propagation, but it could take a huge computing resource to calculate the Huygens–Fresnel integration in the X-ray region. Using a Fourier optics approach, *SRW* (Chubar *et al.*, 2002) efficiently simulates X-ray propagation along beamlines, starting from the radiation source, with electron emittance and energy spread included in a large number of X-ray samplings using the Monte Carlo method.

To quantitatively describe X-ray beam wavefront distortion by crystals, we propagate the wavefront downstream of the monochromator through a 'perfect thin lens' to make a 1:1 focus of the undulator source. Compared with the focus without considering crystal deformation, any increase of the focal size represents a degree of wavefront distortion, and implies an increase of future nano-focusing size with nano-focusing optics. From this perspective, the incident beam onto future focusing optics after the monochromator is equivalent to the beam coming from a source with equal dimensions of these simulated 1:1 images but with a perfect monochromator. For helical undulators, wavefront simulations are performed under the worst thermal load condition with $Kx = Ky = 0.707$. For planar undulators, the wavefront simulations are performed at a more realistic condition with the first harmonic at 8 keV, rather than the highest heat load condition with the first harmonic at 3.6 keV.

Table 5
Simulation of 1:1 focusing of ERL beamlines.

Undulator type	First-harmonic energy (keV)	Current (mA)	Residual error (Å)†	Focus without deformation		Focus with deformation	
				$FWHM_x$ (μm)	$FWHM_y$ (μm)	$FWHM_x$ (μm)	$FWHM_y$ (μm)
5 m planar	8.0	25	1.81/0.20	12.9	12.6	12.9	12.7
	8.0	100	6.77/0.78	15.4	14.4	15.9	15.2
25 m planar	8.0	25	1.94/0.23	28.4	27.5	28.7	27.4
	8.0	100	3.74/0.59	35.0	32.4	35.1	34.0
5 m helical	8.32	25	1.11/0.18	13.1	12.9	13.2	12.9
	8.32	100	4.74/0.77	15.4	14.2	15.6	14.7
25 m helical	8.32	25	1.31/0.19	28.8	27.9	29.2	27.8
	8.32	100	4.71/0.74	34.7	32.1	34.8	33.2

† Peak-to-valley/RMS values of the thermal displacement after subtraction of toroidal curvatures.

As shown in Figs. 6(*a*) and 6(*c*), the ERL monochromator thermal deformations within the footprint area can be fitted with toroidal curvatures, with residual difference only in the range of angströms, as shown in Figs. 6(*b*) and 6(*d*) and in Table 5. While the wavefront change by the toroidal curvatures can be compensated by adjusting the downstream optics focus, the changes arising from the residual figure errors may not be easily correctable and are simply treated as an increase of focal sizes as the worst possible scenario in this paper. In *SRW* terminology, multiple optical components can be integrated into an optical 'container', and in our case this container contains (i) the phase object determined by the crystal deformation output from *ANSYS*, and (ii) the 1:1 focusing thin lens. Without considering crystal deformation, the focal length of the thin lens will be just half of the distance from lens to source. Because of the focusing effect by the toroidal curvature of the Si crystal, the actual focal length of the thin lens needed for the 1:1 focusing can be calculated through the compound lens equation and mirror focusing equations (Howell & Horowitz, 1975) as

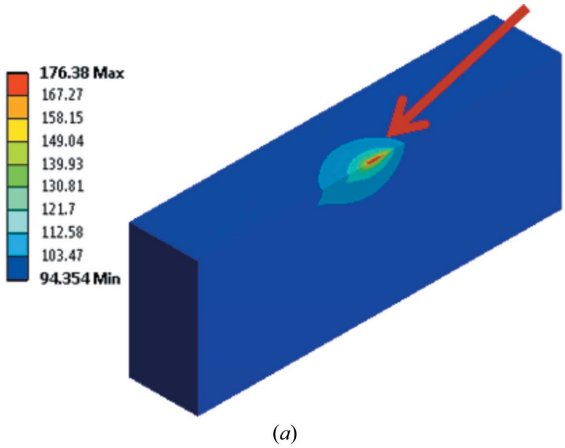

(*a*)

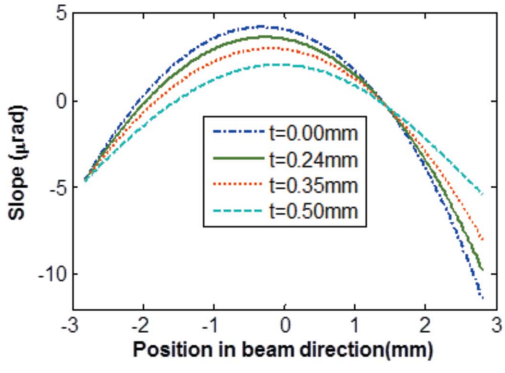

(*b*)

Figure 7
ANSYS results for Si crystal temperature (*a*) and slope errors at different sagittal positions, *t*, within the footprint (*b*) for a monochromator at 55 m from the source, for a 25 m planar undulator beamline working at K = 2.22, with machine current of 100 mA. With Si(111) set to the third harmonic, the maximum temperature is 176 K, the maximum displacement within the footprint area is 12.6 nm, and the intensity-weighted slope error is 3.4 μrad. The incident beam direction is shown with a red arrow.

$$1/f_s = 1/f_0 - 2\sin(\alpha)/R_s, \tag{7}$$

$$1/f_t = 1/f_0 - 2/\left[R_t \sin(\alpha)\right], \tag{8}$$

where R_s and R_t are the least-squares fitted radii of the crystal curvatures along the sagittal and meridional directions, with positive values for concave deformations, and f_0 is the thin-lens focal length required without considering crystal deformation, which is half of the distance to the source. With (7) and (8), the thermal deformed crystal and the thin lens will work together to focus the source at a 1:1 magnification ratio, imaging the source at a distance of $2f_0$ downstream of the lens. For simplicity, the distance between crystal and thin lens is assumed to be zero. Because least-squares fitting treats each fitting data with equal weight while the X-ray intensity distribution is not uniform over the footprint, using the fitted R_s, R_t and equations (7) and (8) may not give us the smallest focal size. Small 'improvements of focusing' are achieved by adjusting f_t slightly for high flux mode situations, selecting the best result from multiple simulations with slightly different f_t. However, for the lower current high-coherence mode, because the crystal thermal curvatures (reciprocal of radii) are small, there is no need to adjust the least-squares fitted radii for *SRW* simulations.

Fig. 8 shows the simulated changes of 1:1 focusing for all helical undulator beamlines, working at the highest possible thermal load condition with K = 0.707, and for all planar undulators with the first harmonic at 8 keV. It can be seen that, when the ERL runs in the high coherence mode with a current

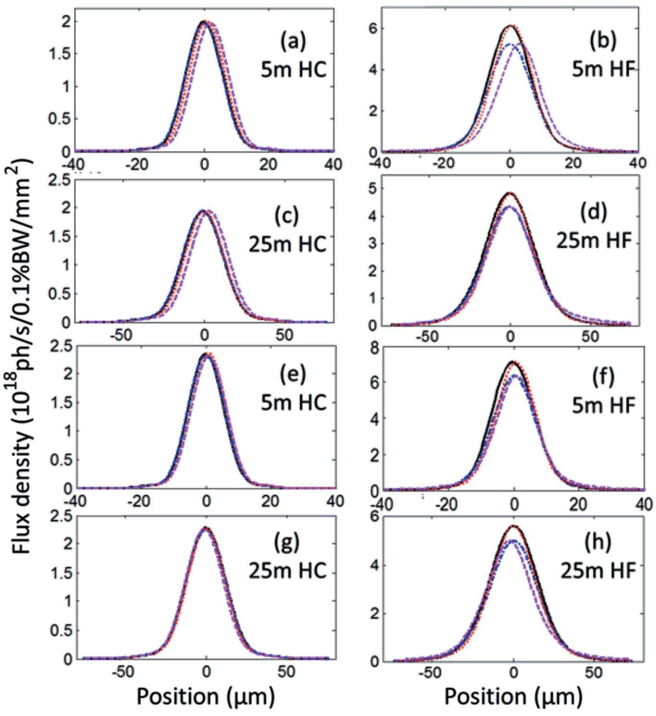

Figure 8
Wavefront simulations of 1:1 focusing of ERL undulator sources. In each figure the solid and dotted lines are the horizontal and vertical profiles without considering crystal thermal deformation, and the dash-dotted and dashed lines are the corresponding profiles considering crystal thermal deformation. (*a*) to (*d*) are for planar undulators with first harmonic at 8 keV, and (*e*) to (*h*) are for helical undulators with first harmonic at 8.33 keV, the maximum on-axis power condition. In the legend, 5 m and 25 m are the length of the undulators, and HC and HF stand for high coherence and high flux modes, respectively.

of 25 mA, there are almost no changes of simulated focus size with and without considering wavefront deformation of the monochromator crystal. For the ERL running in high flux mode of 100 mA, there are only minor changes of the simulated focusing with and without considering crystal deformations. The increase of focal size is more noticeable in the vertical than horizontal directions, as summarized in Table 5. The deformation asymmetry caused by volume heat load also causes a slight 'detuning' of the crystal, and such detuning is adjusted in the wavefront simulation by 'rotating' the crystal to compensate. The shift of the vertical focusing profiles in Fig. 8 come from the residual errors after such adjustment.

6. Conclusion

The Cornell ERL undulator beamlines will have high on-axis power density, but the total power within the central cones is comparable with undulator beamlines of third-generation sources. The modified linear power density is typically no more than 100 W mm^{-1} for ERL cryogenic cooled Si(111) monochromators. The slope errors caused by such thermal deformations are comparable with what is observed at third-generation beamlines and in general very small compared with the crystal rocking curve width. For planar undulators working at 8 keV and helical undulators working at 8.33 keV, wavefront simulation of 1:1 focusing of ERL sources shows wavefront deformation to be either negligible or minor. Thus, generally speaking, the present design of cryogenically cooled Si monochromators is quite suitable for high power density and highly coherent ERL beamlines.

RH acknowledges help from Dr Oleg Chubar for the use of *SRW*. Valuable suggestions from Professor Ivan Bazarov and Dr Darren Dale are appreciated. CHESS is supported by the NSF and NIH/NIGMS *via* NSF awards DMR-0936384 and NSF DMR-0807731.

References

Balewski, K. (2008). *16th European Synchrotron Light Source Workshop*, Daresbury, UK, November 2008.
Bazarov, I. (2012). *Phys. Rev. ST Accel. Beams*, **15**, 050703.
Bilderback, D. H., Brock, J. D., Dale, D. S., Finkelstein, K. D., Pfeifer, M. A. & Gruner, S. M. (2010). *New J. Phys.* **12**, 035011.
Chubar, O., Elleaume, P., Kuznetsov, S. & Snigirev, A. (2002). *Proc. SPIE*, **4769**, 145–151.
Chumakov, A., Rüffer, R., Leupold, O., Celse, J.-P., Martel, K., Rossat, M. & Lee, W.-K. (2004). *J. Synchrotron Rad.* **11**, 132–141.
Dejus, R. J., Vasserman, I. B., Sasaki, S. & Moog, E. R. (2002). Argonne National Laboratory Report ANL/APS/TB-45. Argonne National Laboratory, Argonne, IL, USA.
Freund, A. K., Hoszowska, J., Migliore, J. S., Mocella, V., Zhang, L. & Ferrero, C. (2000). *AIP Conf. Proc.* **521**, 247–252.
Hoszowska, J., Mocella, V., Zhang, L., Migliore, J. S., Freund, A. & Ferrero, C. (2001). *Nucl. Instrum. Methods Phys. Res. A*, **467–468**, 631–634.
Howell, J. A. & Horowitz, P. (1975). *Nucl. Instrum. Methods*, **125**, 225–230.
Huang, R. & Bilderback, D. H. (2012). *Proc. SPIE*, **8502**, 85020B10.
Kazimirov, A., Revesz, P. & Huang, R. (2008). *Proc. SPIE*, **7077**, 707702.
Kim, K.-J. (1988). *AIP Conf. Proc.* **184**, 565–633.
Lee, W.-K., Fernandez, P. & Mills, D. M. (2000). *J. Synchrotron Rad.* **7**, 12–17.
Mocella, V., Ferrero, C., Freund, A., Hoszowska, J., Zhang, L. & Epelboin, Y. (2001). *Nucl. Instrum. Methods Phys. Res. A*, **467–468**, 414–417.
Mocella, V., Lee, W.-K., Tajiri, G., Mills, D., Ferrero, C. & Epelboin, Y. (2003). *J. Appl. Cryst.* **36**, 129–136.
Nesterets, Y. (2008). *Opt. Commun.* **281**, 533–542.
Nugent, K. A. (2010). *Adv. Phys.* **59**, 1–99.
Nugent, K. A., Tran, C. Q. & Roberts, A. (2003). *Opt. Express*, **11**, 2323–2328.
Onuki, H. & Elleaume, P. (2003). *Undulators, Wigglers and their Applications.* London: Taylor and Francis.
Robinson, I. K., Kenney-Benson, C. A. & Vartanyants, I. A. (2003). *Physica B*, **336**, 56–62.
Rogers, C. S., Mills, D. M., Fernandez, P. B., Knapp, G. S., Wulff, M., Hanfland, M., Rossat, M., Freund, A., Marot, G., Holmberg, J. & Yamaoka, H. (1996). *Rev. Sci. Instrum.* **67**, 3350.
Tajiri, G., Lee, W.-K., Fernandez, P., Mills, D. M., Assoufid, L. & Amirouche, F. (2001). *J. Synchrotron Rad.* **8**, 1140–1148.
Tamasaku, K., Yabashi, M., Miwa, D., Mochizuki, T. & Ishikawa, T. (2002). *Proc. SPIE*, **4782**, 132–142.
Tanaka, T. & Kitamura, H. (2001). *J. Synchrotron Rad.* **8**, 1221–1228.
Temnykh, A. B. (2008). *Phys. Rev. ST Accel. Beams*, **11**, 120702.
Vartanyants, I. A. & Robinson, I. K. (2003). *Opt. Commun.* **222**, 29–50.

Walker, R. P. (1998). *CERN Accelerator School*, CERN-98–04, pp. 129–190. CERN, Switzerland.
Wiedemann, H. (2003). *Particle Accelerator Physics I: Basic Principles and Linear Beam Dynamics*, 2nd ed., pp. 325–326. Berlin: Springer.
Zhang, L., Lee, W.-K., Wulff, M. & Eybert, L. (2003). *J. Synchrotron Rad.* **10**, 313–319.
Zhang, L., Sánchez del Río, M., Monaco, G., Detlefs, C., Roth, T., Chumakov, A. I. & Glatzel, P. (2013). *J. Synchrotron Rad.* **20**, 567–580.